


Technical Note

Pre-Archaeological Investigation by Integrating Unmanned Aerial Vehicle Aeromagnetic Surveys and Soil Analyses

Wei Cao ¹, Hao Qing ², Xing Xu ³, Chang Liu ⁴, Silin Chen ⁴, Yi Zhong ^{1,5}, Jiabo Liu ¹, Yuanjie Li ¹, Xiaodong Jiang ¹, Dalun Gao ⁶, Zhaoxia Jiang ^{7,8} and Qingsong Liu ^{1,5,9,*}

- ¹ Centre for Marine Magnetism (CM2), Department of Ocean Science and Engineering, Southern University of Science and Technology, Shenzhen 518055, China
- ² GTK (Shenzhen) Technology Co., Ltd., Shenzhen 518102, China
- ³ Guangzhou Marine Geological Survey, Guangzhou 510760, China
- ⁴ Guangdong Provincial Institute of Cultural Relics and Archaeology, Guangzhou 510075, China
- ⁵ Laboratory for Marine Geology, Pilot National Laboratory for Marine Science and Technology, Qingdao 266061, China
- ⁶ SUSTech Academy for Advanced Interdisciplinary Studies, Shenzhen 518055, China
- ⁷ Frontiers Science Center for Deep Ocean Multispheres and Earth System, Key Laboratory of Submarine Geosciences and Prospecting Techniques, Ministry of Education, College of Marine Geosciences, Ocean University of China, Qingdao 266100, China
- ⁸ Laboratory for Marine Geology, Laboratory for Marine Mineral Resources, Qingdao National Laboratory for Marine Science and Technology, Qingdao 266237, China
- ⁹ Southern Marine Science and Engineering Guangdong Laboratory (Guangzhou), Guangzhou 511458, China
- * Correspondence: qslu@sustech.edu.cn



Citation: Cao, W.; Qing, H.; Xu, X.; Liu, C.; Chen, S.; Zhong, Y.; Liu, J.; Li, Y.; Jiang, X.; Gao, D.; et al.

Pre-Archaeological Investigation by Integrating Unmanned Aerial Vehicle Aeromagnetic Surveys and Soil Analyses. *Drones* **2022**, *6*, 243.

<https://doi.org/10.3390/drones6090243>

Academic Editor: Diego González-Aguilera

Received: 15 August 2022

Accepted: 3 September 2022

Published: 6 September 2022

Publisher's Note: MDPI stays neutral with regard to jurisdictional claims in published maps and institutional affiliations.



Copyright: © 2022 by the authors. Licensee MDPI, Basel, Switzerland. This article is an open access article distributed under the terms and conditions of the Creative Commons Attribution (CC BY) license (<https://creativecommons.org/licenses/by/4.0/>).

Abstract: Magnetic surveys have been widely used in archaeological field investigations. However, conventional survey methods are often restricted by complicated field conditions and ambiguities in data interpretation. In this study, a novel magnetic survey system was designed for pre-archaeological investigation (preliminary survey prior to the archaeological excavation) based on a modified quadrotor unmanned aerial vehicle (UAV) and was successfully applied to an archaeological area with a complex landform in Huizhou, China. Results show that the target anomaly identified by UAV aeromagnetic survey corresponds well to the location of a potential archaeological site. Subsequent soil analyses further confirm the archaeological value of UAV aeromagnetic results and provide strong constraints on the interpretation of target anomalies. This study demonstrates that the newly proposed UAV aeromagnetic system can adapt to the various field conditions with the advantages of flexibility and efficiency, which has great potential for future archaeological investigations.

Keywords: unmanned aerial vehicle; pre-archaeological investigation; integrated method; aeromagnetic survey; soil analyses

1. Introduction

Pre-archaeological investigations (e.g., geophysical survey and soil analysis) [1–3] are crucial for archaeological studies [4–6]. As a non-destructive, efficient, and repeatable geophysical method, magnetic surveys based on the magnetization contrast between the target and background have been widely used in archaeological exploration [2,5,7–11]. More specifically, archaeological sites often exhibit distinct magnetization characteristics compared to the natural background because of alterations by human activities [12–15]. Therefore, potential archaeological targets can often be detected by magnetic anomalies [16–18]. However, conventional magnetic surveys in archaeological practice mainly use manual ground-based survey methods, which are often restricted by complicated field conditions and the ambiguities inherent in data interpretation [2,6,19].

In terms of the soil properties, soil analysis is also an intuitive survey method in archaeological studies [20]. Ancient human activities can modify the natural sedimentary

processes and then alter soil properties [3,14,15,21]. Therefore, it is possible to identify ancient human traces by analyzing changes in soil properties. However, soil properties are often complex because of the various different archaeological site types (e.g., walls, houses, and stoves) reflecting different human activities [2,3,21]. Systematic soil analyses are needed to precisely determine the origin of the soil and provide more constraints to interpret magnetic survey data.

With the development of advanced equipment and soil analysis methods, pre-archaeological surveys can be further improved. For example, as an emerging flight platform, unmanned aerial vehicles (UAV) equipped with magnetometers for aeromagnetic surveys adapt to complex field conditions, with the advantages of intelligence, flexibility, automation, and efficiency [22–26]. New analytical methods from multiple disciplines can extract the diverse properties of soil samples (e.g., rock magnetism, environmental magnetism, sedimentology, and geochemistry) [3,20,21,27–29]. More importantly, a combined approach by integrating these multidisciplinary techniques can efficiently reduce ambiguities in data interpretation of any single method [6,19].

In this study, we combine UAV aeromagnetic surveys and soil analyses for archaeological field investigation. To test the feasibility of the method, aeromagnetic scanning was performed in a potential archaeological area in Huizhou, China. Rock magnetic properties, sedimentary environment, and provenance information of the soil profiles from both the potential archaeological site and the background area were conducted. Our results demonstrate the potential archaeological value of this target, as well as the success of the combined method for pre-archaeological surveys.

2. Geological and Archaeological Background

Huizhou, located in the southeastern Guangdong Province ($22^{\circ}24' \text{ N}$ – $23^{\circ}59' \text{ N}$, $113^{\circ}51' \text{ E}$ – $115^{\circ}28' \text{ E}$), is the northeastern part of the Pearl River Delta (Figure 1). This region has a well-developed water system, fertile soil, and abundant mineral and forest resources [30]. Tectonic activities in Huizhou have been limited since the late Quaternary [31,32], and Huizhou is strategically important for the eastern development of the central plains civilization and a battleground for military strategists [33,34]. The Fulou state was once established in the ancient Huizhou area, but its city site and territorial area were only roughly recorded in the ancient texts and thus further detailed research is required. Magnetic surveys and archaeological research in this area will thus help to further uncover the mystery of the ancient Fulou civilization that disappeared thousands of years ago [35].



Figure 1. Topography and location of the study site. (a) Topographic of Huizhou: the blue block is the Huizhou area, the red circle indicates survey location; (b) location of the study area in the world: the blue star indicates relative position.

3. Materials and Methods

3.1. UAV Aeromagnetic System

The magnetic survey mode was designed according to the actual situation and environment of the study area. This area is located in a potential archaeological site with a subtropical monsoon climate, and the landform is covered by tall vegetation and dense jungle. There are also several private plantations in this region. These complex environments make it extremely difficult to carry out conventional ground surveys. Therefore, in this study, a flexible and intelligent UAV platform is selected to overcome the complex landforms. After official authorization and approval, the aeromagnetic surveys were designed and carried out under the premise of ensuring safety (at the minimum safe altitude for UAV flying in the survey area).

A GTK-RF-M300 UAV aeromagnetic system developed in conjunction with GTK Technology Co., Ltd. (Shenzhen, China) was used in this study (Figure 2). This system consists of different modules: data acquisition, flight platform, ground base station, data processing, and quality control (Table 1). The DJI M300 RTK multi-rotor UAV is equipped with a horizontal carbon fiber tube (Figure 2a), and it is optional to mount one (at either end of the tube) or two (at both ends of the tube) magnetometers. In this study, the single (chip-level atomic optical pump) magnetometer mode (Figure 2c) was used for the aeromagnetic survey, while the other magnetometer was installed on the ground in the magnetic survey area as a magnetic diurnal station for data post-correction processing. The data acquisition module is hard-connected with the UAV through a carbon fiber tube (Figure 2b), and the direction the UAV faces is kept consistent during each aeromagnetic survey.

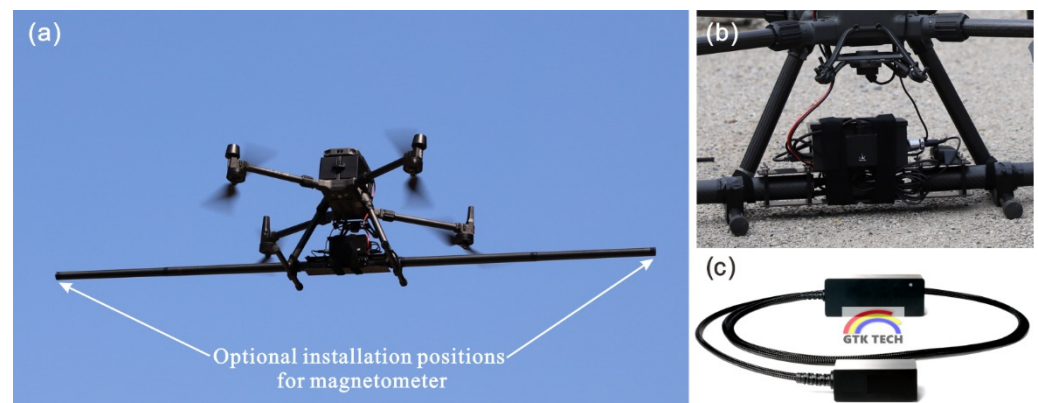


Figure 2. Multi-rotor UAV aeromagnetic system GTK-RF-M300. (a) Automatic flight mode of aeromagnetic system; (b) integration module; (c) magnetometer.

Table 1. Performance of the UAV aeromagnetic system.

| Module | Index | Performance |
|-----------------------------------|---------------------------|---|
| Magnetic module (magnetometer) | Type | Total magnetic field intensity |
| | Resolution | 0.0001 nT |
| | Sensitivity | Better than 0.02 nT/ $\sqrt{\text{Hz}}$ |
| | Range | 1000 nT–100,000 nT |
| | Gradient tolerance | Maximum 100 nT/cm |
| | Blind zone | Single equatorial plane ± 7 degrees |
| | Mount position | At the end of carbon fiber tube (1.5 m) |
| | Noise level (hover state) | 0.02 nT (fourth-order difference) |
| | Sampling rate | Four optional modes (1, 2, 5, 10 Hz) |
| | Power consumption | 5 V, 3 W |
| Operating temperature | -30 °C to $+60$ °C | |

Table 1. Cont.

| Module | Index | Performance |
|------------------------------|----------------------|---|
| Flight platform module (UAV) | Positioning accuracy | Horizontal ± 1.25 m (GPS) Vertical ± 0.1 m (laser altimeter) |
| | Flight endurance | Maximum 55 min |
| | Takeoff weight | Maximum 9 kg (recommend) |
| | Wind resistance | Maximum 15 m/s |
| | Obstacle avoidance | Vision and infrared |

The raw aeromagnetic data (T_{measured}) are corrected according to the international geomagnetic reference field (IGRF) and diurnal variation to calculate the aeromagnetic anomaly $\Delta T = T_{\text{measured}} - T_{\text{IGRF}} - T_{\text{diurnal variation}}$. T_{IGRF} is calculated by the IGRF model [36] at the survey location, which is used to remove the background value of the (Earth's) internal magnetic field. The ground base station measures diurnal variation synchronously with the aeromagnetic surveys, and the amplitude of diurnal variation at the corresponding (survey) time is extracted as $T_{\text{diurnal variation}}$ to eliminate geomagnetic field variation and external interference (e.g., solar activity) [37]. Data from individual survey lines were subsequently interpolated (minimum curvature) onto a regular grid for visualization, and reduction-to-the-pole (RTP) was used to eliminate the effect of oblique magnetization [38].

3.2. Field Sampling

Based on the aeromagnetic survey and field exploration results (Figure 3a), field sampling sites were selected. The location of the magnetic anomaly G corresponds well to a special square area (Figure 3c,d). Therefore, anomaly and background areas were selected in and outside the special square area to study the potential archaeological target and the natural (background) sediments, respectively. Previous excavations of the surrounding sites indicate that the depth of the archaeological sites generally did not exceed 2–3 m below the surface. To conduct a more in-depth investigation of the target area, we used archaeological probes (Figure 3b) to collect deep samples at selected sites. In this study, two representative cores were drilled from the anomaly area (3 m below the surface, blue star in Figure 3c,d) and background area (3.5 m below the surface, green star in Figure 3c,d), respectively. After recovery, samples were sorted, standard packaged, weighed, and then analyzed by laboratory experiments (magnetism, sedimentology, and geochemistry).

3.3. Experimental Methods

Mass-specific magnetic susceptibility (χ) values were measured at dual frequencies, low-frequency χ (χ_{lf} , 976 Hz) and high-frequency χ (χ_{hf} , 15,616 Hz), by using a multi-function Kappabridge system (MFK2-FA, AGICO Ltd.). Frequency susceptibility ($\chi_{\text{fd}}\%$) is defined as $\chi_{\text{fd}}\% = (\chi_{\text{lf}} - \chi_{\text{hf}}) / \chi_{\text{lf}} \times 100\%$. Anhysteretic remanent magnetization (ARM) was determined by a direct current (DC) biasing field (0.05 mT) superimposed on a smoothly decreasing (100 mT as peak) alternating field (AF). Anhysteretic susceptibility (χ_{ARM}) was calculated by ARM/DC (0.05 mT). Isothermal remanent magnetization (IRM) was acquired by a DC field (induced by a 2G model 660 pulse magnetization meter). The saturation IRM_{1T} (SIRM) was imparted at 1 T, and then was demagnetized at 100 mT (IRM_{-0.1T}) and 300 mT (IRM_{-0.3T}), respectively. S-ratio (S_{-0.3T}) was defined as $\text{IRM}_{-0.3T} / \text{SIRM}$.

Temperature-dependent magnetic susceptibility (χ -T) curves were measured by an alternating field of 200 A/m at 976 Hz frequency from room temperature to 700 °C under an argon atmosphere (MFK2-FA, AGICO Ltd.). A vibrating sample magnetometer (VSM) 8600 system (Lake Shore Cryotronics, Inc., Westerville, OH, USA) was used to measure hysteresis loops, IRM acquisition curves, back-field demagnetization curves, and first-order reversal curves (FORCs). Saturation magnetization (M_s), saturation remanent magnetization (M_{rs}), and coercivity (B_c) were extracted from the hysteresis loops, and the coercivity of remanence (B_{cr}) was obtained from backfield demagnetization curves (between +1 T and -1 T). IRM acquisition curves were measured with nonlinear field steps up to 1.5 T,

and then decomposed by the pyIRM software [39]. FORCs were measured with a field increment of 2 mT, and then processed by FORCinel v3.06 software [40].

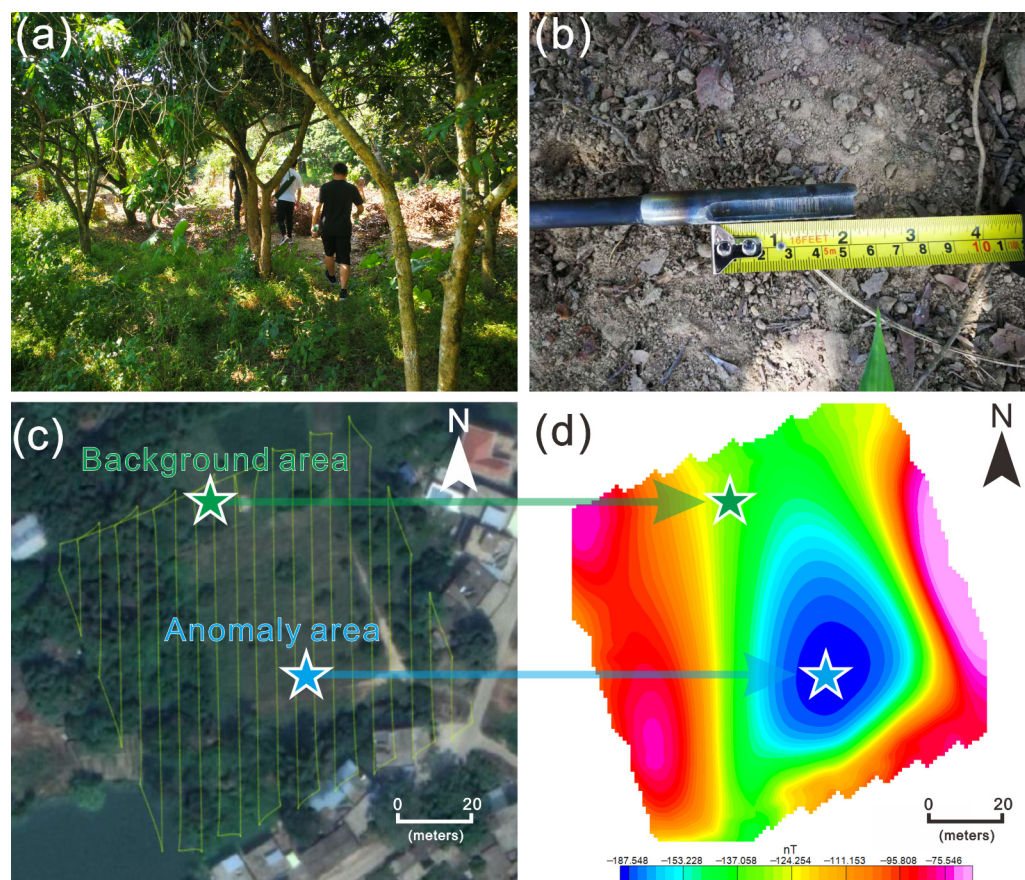


Figure 3. Sampling procedures and sites. (Green star indicates sampling site in background area; blue star indicates sampling site in anomaly area.) (a) Field exploration in complex environment; (b) archaeological probe; (c) sampling sites in aerial photo; (d) sampling sites in RTP magnetic anomaly.

Grain-size distribution (median grain size) was determined by a laser particle sizer (Malvern Mastersizer 3000). Soil samples were processed following the standardized pretreatment (land samples) before the measurement of grain-size distribution, the H_2O_2 and HCl were used to remove organic matter and carbonates, respectively. All chemical pretreatments were carried out in the water bath state with full reaction. After each step of pretreatment, deionized water was used to remove reagent residues.

The concentration index for hematite and goethite was obtained by visible diffuse reflectance spectroscopy (DRS) measurements. A Varian Cary 5000 spectrophotometer equipped with a BaSO_4 -coated integrating sphere was used to scan samples from 400 to 700 nm wavelengths (0.5 nm steps, 300 nm/min scan speed rate), and BaSO_4 was used as the white standard. The DRS data was processed and calculated by the Varian instrument software with smoothed (Savitzky–Golay method), raw data was transformed into Kubelka–Munk (K-M) functions by $[(1 - R)^2/2R]$, where R is the reflectance [41]. Second-derivative curves of the Kubelka–Munk functions were used to extract characteristic coordinates and the concentration index for hematite and goethite.

For geochemical analyses, samples were dissolved before the measurements. First, sample powder (0.05 g) and reagents (0.5 mL HF, 0.5 mL HNO_3 , and 1.5 mL HCl) were digested in a Teflon bottle; second, bottles were sealed and placed on a hot plate (120 °C) for heating for about 12 h; third, when the sample powder was heated to dryness, reagents (1 mL HNO_3 and 1 mL H_2O) were added; and fourth, bottles were sealed again and placed on a hot plate (150 °C) for dissolving the residue phase for about 12 h. Major elements

were analyzed by a Thermo-Fisher IRIS II Intrepid XSP ICP-OES. Trace elements and rare earth were measured by a PerkinElmer ELAN 9000 ICP-MS (inductively coupled plasma mass spectrometry). Internal calibration reference materials (GBW07315, GBW07316, BCR-2, BHVO-2, GBW07295, GBW07296, NOD-P-1, and NOD-A-1) were used to correct the measured data.

The experimental analyses of soil samples were carried out by laboratory instrumentations. Geochemical measurements were performed at the Institute of Oceanology, Chinese Academy of Sciences. All other measurements were performed at the Southern University of Science and Technology, China.

4. Results

4.1. UAV Aeromagnetic Anomaly

The study area, designated by the archaeological cooperation team, is outlined by regular edges that form a square shape (Figure 4b,d), which is consistent with the specifications and concepts of ancient Chinese cities and walls [42,43]. To further investigate this area, two aeromagnetic surveys (line spacing 5 m, data interval along line 1.6 m) were conducted along different directions (20 survey lines each in the north–south and west–east directions).

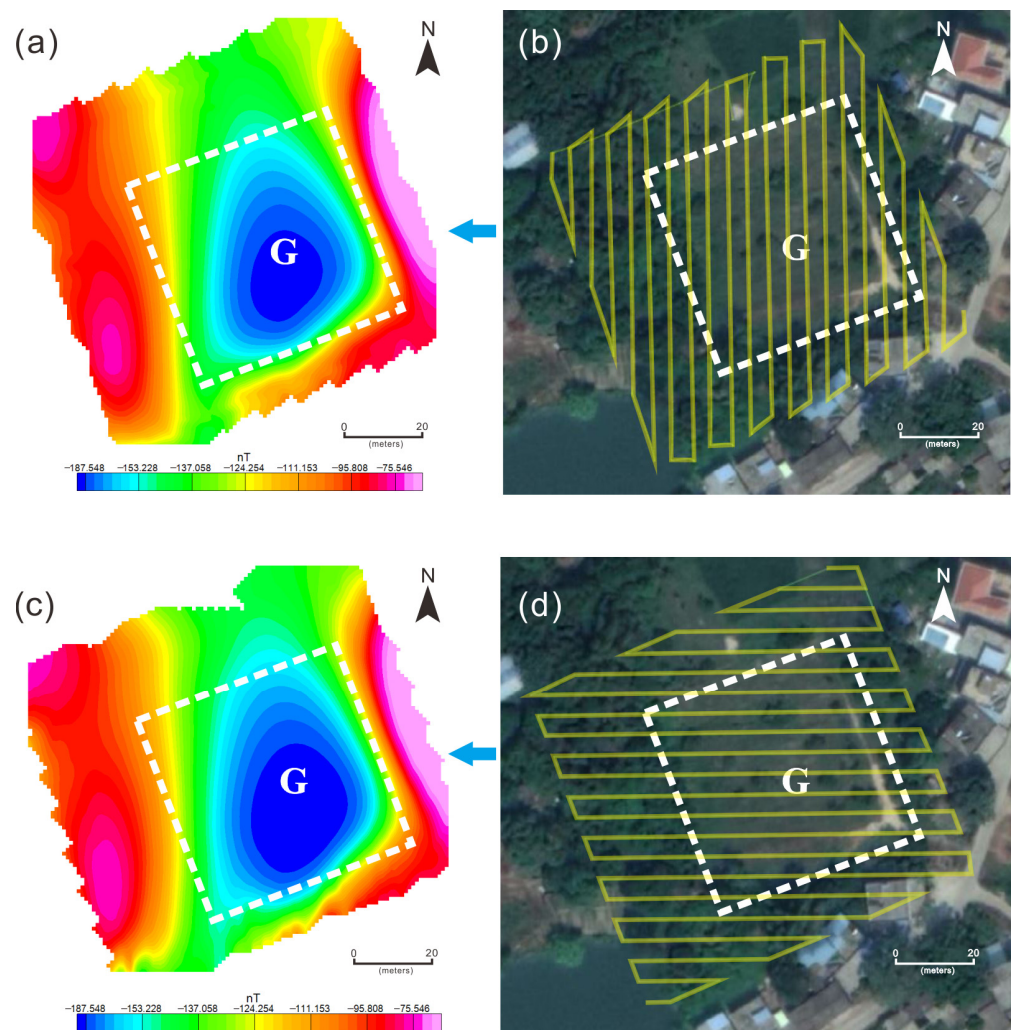


Figure 4. Aeromagnetic results and anomaly identification of the survey area (yellow lines indicate survey lines). (a) Distribution of RTP magnetic anomalies along the north–south survey line; (b) distribution of landforms, architecture, and north–south survey line in the aerial photo; (c) distribution of RTP magnetic anomalies along the west–east survey line; (d) distribution of landforms, architecture and west–east survey lines in the aerial photo.

During the aeromagnetic measurement, the UAV was set at a constant cruise speed to ensure the accuracy of data intervals along lines, and the flights were executed in mild weather to reduce wind interference. Flight sensors collected, recorded, and outputted data synchronously. Comprehensive quality control of the aerial survey data (Table 2) was performed by monitoring the statistics of flight speed, number of output data per second, survey line spacing, data interval along a line, average flight height, altitude standard deviation (including vegetation), and the dynamic noise (referring to the combined noise during aeromagnetic surveying).

Table 2. Statistics of flight quality index.

| Flight Quality Index | Survey Along North–South Line | Survey Along West–East Line |
|----------------------------------|-------------------------------|-----------------------------|
| Average flight speed (m/s) | 8 | 8 |
| Number of output data per second | 5 | 5 |
| Survey line spacing (m) | 5 | 5 |
| Data interval along line (m) | 1.6 | 1.6 |
| Average flight height (m) | 28.3 | 28.3 |
| Altitude standard deviation | 4.5 | 4.2 |
| Dynamic noise (nT) | 0.0973 | 0.0954 |

After data processing, the square geomorphic G area appears as an isometric negative (compared with background) anomaly center in the RTP magnetic field with a consistent morphological position (Figure 4a,c). The consistent response of two surveys (along different directions) supports the fidelity of the magnetic anomaly related to the square landform (G area).

4.2. Magnetic Mineralogy

Magnetic mineral concentrations can be quantified by χ , χ_{ARM} , and SIRM, with high values indicating higher concentrations of magnetic minerals. χ is contributed to by all kinds of magnetic minerals (diamagnetic, paramagnetic, ferrimagnetic, and antiferrimagnetic) in the sediment [44]. χ_{ARM} is sensitive to the concentration of ferrimagnetic minerals in stable single domains (SSD) and fine pseudo-single domains (PSD) [28], while SIRM is carried by magnetic particles coarser than the nano-sized superparamagnetic (SP) particles [27]. For each area, χ , χ_{ARM} , and SIRM have similar trends, which indicates that these parameters are controlled dominantly by magnetic mineral concentrations (Figure 5a–c). In the background area, the magnetic mineral concentration peaks at approximately 25–50 cm below the surface (cmbs). In contrast, in the anomaly area, the elevated magnetic mineral concentration occurs at lower depths (at 80–125 cmbs), which results in a strong contrast of magnetic mineral concentrations at the corresponding depth.

$\chi_{fd}\%$ and χ_{ARM} are excellent proxies for superparamagnetic (SP) and SSD particles [45], respectively, while SIRM and χ are sensitive to coarser particles. Thus, $\chi_{ARM}/SIRM$ and χ_{ARM}/χ can be used to reflect magnetic grain size changes [46]. As shown in Figure 5d–f, the magnetic mineral grain size is relatively finer at 50–80 and 80–125 cmbs in the background and anomaly areas, respectively.

Antiferromagnetic minerals can be detected by the S-ratio and hematite (Hm) and goethite (Gt) index (Figure 5g–i). The S-ratio indicates the relative proportions of antiferromagnetic (high coercivity, e.g., hematite and goethite) and ferromagnetic minerals (low coercivity, e.g., magnetite). The higher S-ratio value corresponds to the higher proportion of low-coercivity magnetic minerals, and vice versa [47]. Variations in S-ratio values indicate that the proportion of high coercivity has multiple peaks in the background area but basically keeps a low value in the anomaly area between 25–125 cmbs. Variations in the Hm and Gt index mirror that of the S-ratio.

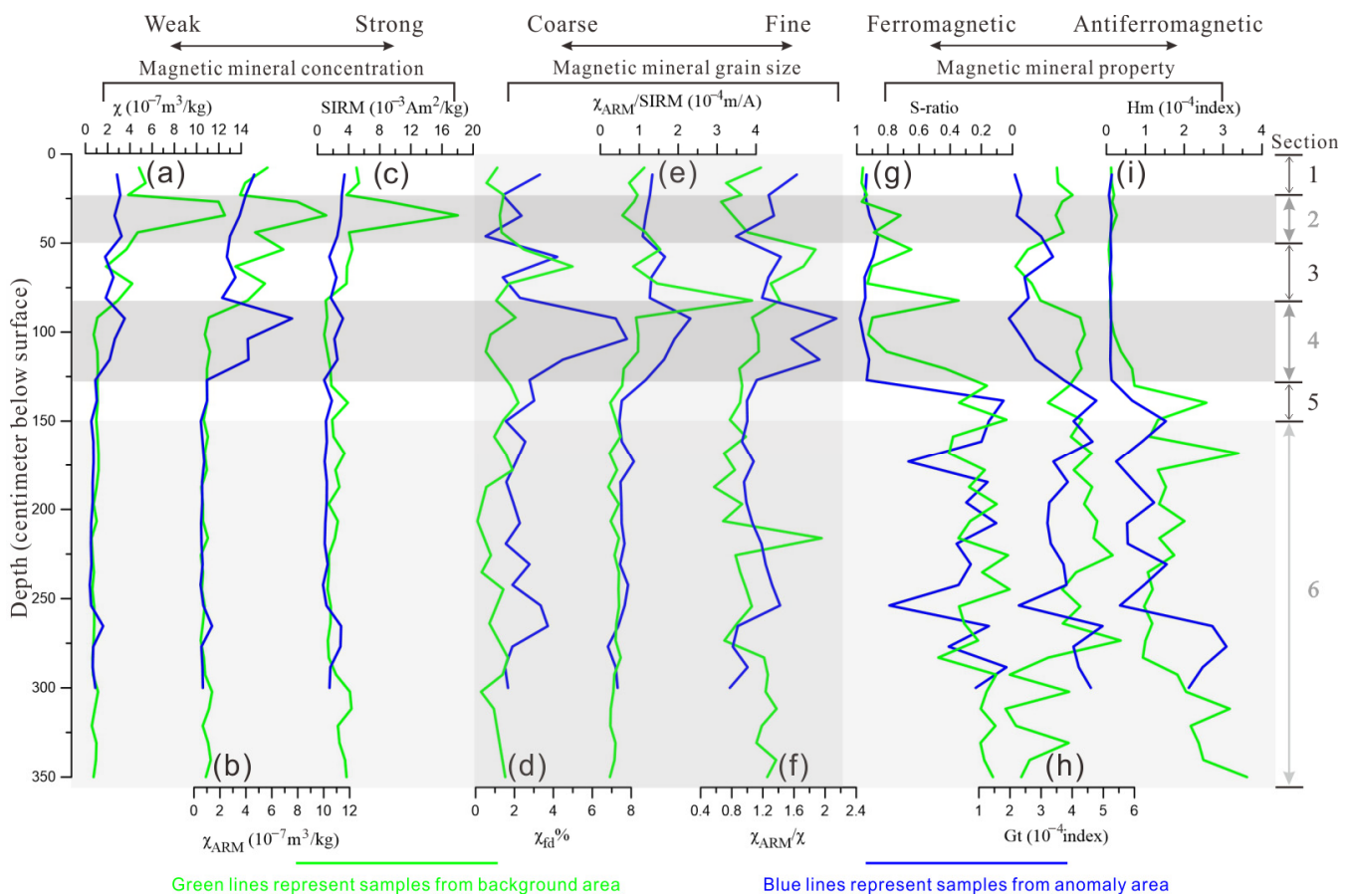


Figure 5. Variation of magnetic concentrations, grain size, and mineralogy parameters with depth. (Green lines represent samples from the background area; blue lines represent samples from the anomaly area. The gray shadings are used to distinguish sections.) (a) χ ; (b) χ_{ARM} ; (c) SIRM; (d) $\chi_{fd}\%$; (e) $\chi_{ARM}/SIRM$; (f) χ_{ARM}/χ ; (g) S-ratio; (h) Gt—goethite index; (i) Hm—hematite index.

On the basis of the magnetic properties, the whole profile can be divided into six sub-sections (Figure 5). Section 1 (0–25 cmbs) exhibits no uniform relationship between the parameter changes, probably because of the surficial disturbances. Section 2 (25–50 cmbs) is characterized by elevated concentration-dependent parameters and coarser grain sizes for the background area. Section 3 (50–80 cmbs) can be regarded as a transition zone between Sections 2 and 4. Compared with Section 2, Section 4 (80–125 cmbs) has higher ARM, $\chi_{fd}\%$, and χ_{ARM}/χ values for the anomaly area, which indicates the presence of a higher number of nano-sized SP and SD magnetic particles. The parameters gradually tend to be similar in Section 5 (125–150 cmbs), which can also be regarded as a transition zone. For Section 6 (>150 cmbs), samples from the anomaly area and the background both have comparable and lower χ , χ_{ARM} , SIRM, and $\chi_{fd}\%$ values. This indicates that Section 6 can be attributed to the C-horizon for typical soil profiles.

4.3. Rock Magnetism

To further determine the magnetic characteristics, representative samples from Section 2 (35 cmbs), Section 4 (90 cmbs), and Section 6 (150 cmbs) were selected. χ -T curves are used to identify the type of magnetic minerals (Figure 6b–g) [48]. In Sections 2 and 4, the heating curve of the background sample decreases significantly at 580 °C and ~700 °C, which indicates the co-existence of magnetite and hematite. In contrast, the heating curve for the anomaly sample indicates the dominance of magnetite. In Section 6, the similar thermomagnetic behavior for both soil profiles indicates similar magnetic mineralogy.

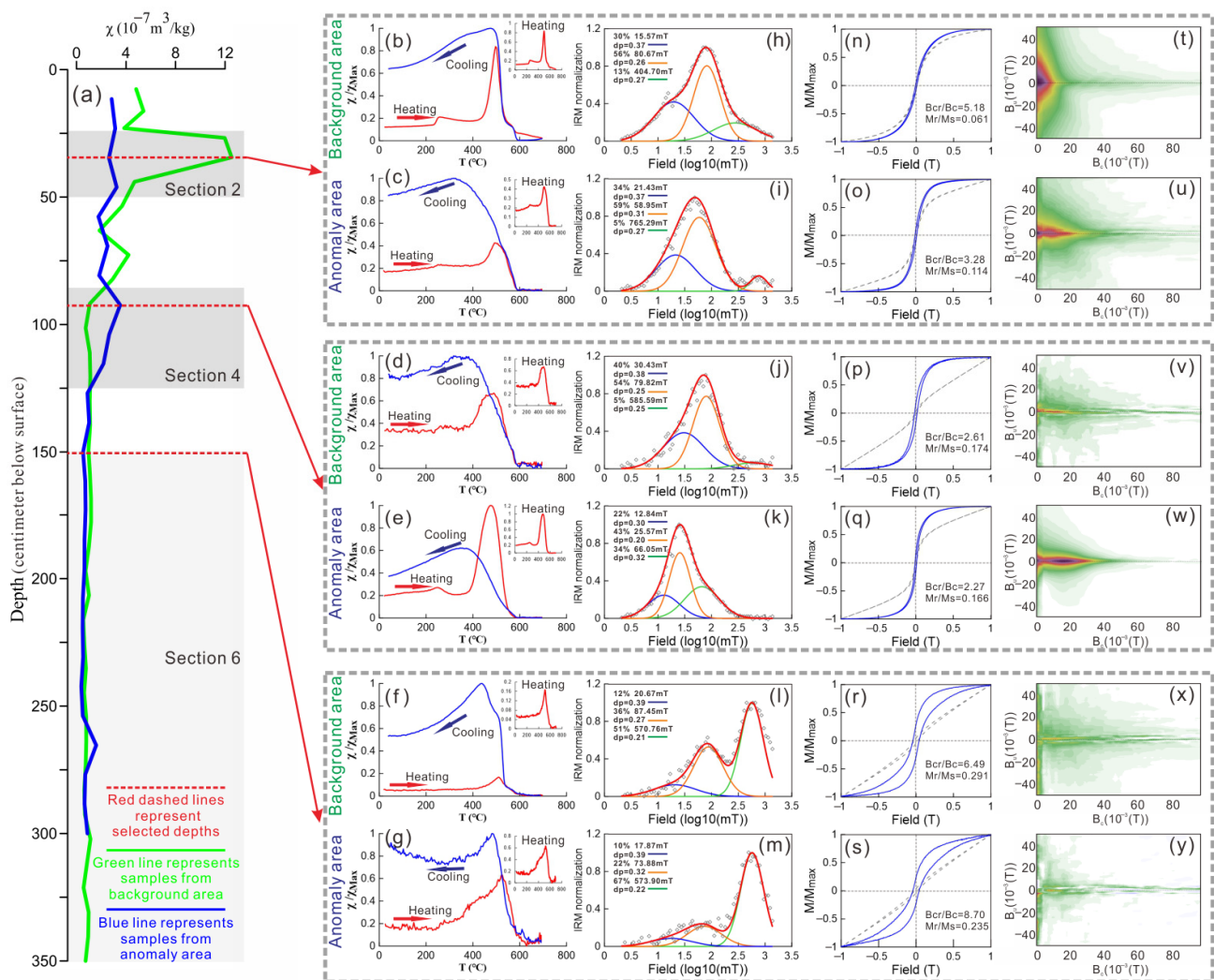


Figure 6. Rock magnetic results of the selected depths (red dashed lines represent selected depths). (a) χ ; (b–g) χ -T curves; (h–m) IRM acquisition curve decomposition (blue, orange, green, and red curves indicate components 1, 2, 3, and the sum of components, respectively); (n–s) magnetic hysteresis loops; (t–y) FORC diagrams.

The decomposition of the IRM acquisition curves can determine the distribution of mineral remanence coercivity [49]. All curves can be fitted with three components (Figure 6h–m). In Sections 2 and 4, the coercivity of the dominant components in the background area is higher than that in the anomaly area. Compared to samples from Sections 2 and 4, in Section 6, the IRM curves are carried by higher coercivity minerals.

Hysteresis loops provide information on both the coercivity and particle size of magnetic minerals (Figure 6n–s) [50]. Generally, in Sections 2 and 4, the lower coercivity values indicate that ferrimagnetic minerals are dominant. In contrast, the wasp-waisted hysteresis loops indicate the coexistence of both ferrimagnetic and antiferromagnetic minerals [51].

FORC diagrams can reflect the domain state and interaction of magnetic particles (Figure 6t–y) [52]. In Section 2, the FORC diagram of the background area shows lower coercivity (<10 mT) with a wider vertical distribution, which indicates that MD particles are dominant, while that of samples from the anomaly area elongates horizontally with vertical spreads ($B_c = 0$), which indicates the existence of PSD particles. In Section 4, the FORC diagram of the background area shows higher coercivity (>20 mT) and vertical spreads ($B_c = 0$), which may indicate PSD particles, whereas the FORC diagram of the anomaly area is characterized by two independent contours, which indicates the coexistence of minerals with two different coercivities. One has a low-coercivity peak at ~ 5 mT, which

indicates fine-grained SD particles, and the other has a smoothly closed contour peak at 10–30 mT, which indicates the presence of stable SD magnetic particles. In Section 6, the FORC diagrams are similar from both areas, which have weak signals and all show a combination of a slender horizontal spread and ultra-low-coercivity vertical distribution, indicating the occurrence of PSD particles or a mixture of SD and SP particles.

4.4. Sedimentary Environment and Provenance

The median particle size of sediments is controlled mainly by the depositional environment, transportation mode, and provenance (Figure 7a) [29]. Overall, samples from both soil profiles have finer grain sizes below 125 cmbs. At shallower depths, the grain sizes increase and show more fluctuated features.

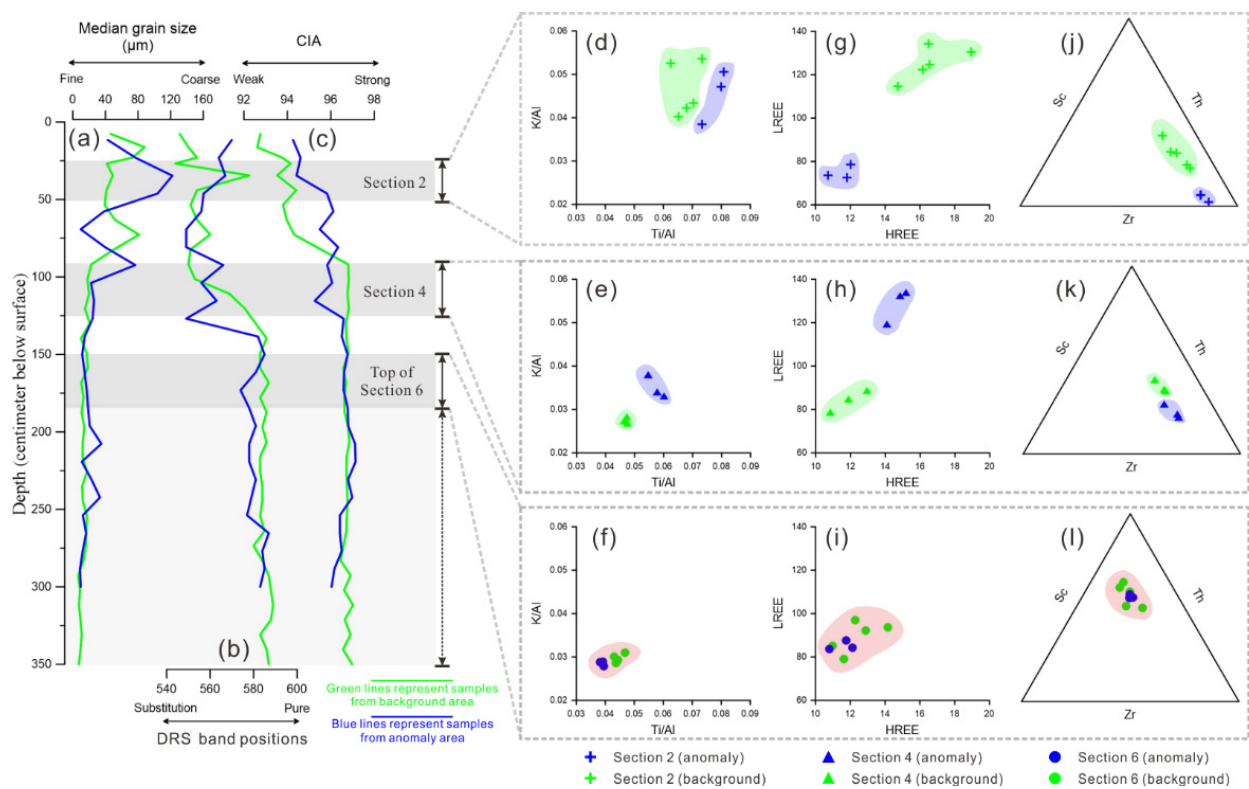


Figure 7. Index of sedimentary environment and provenance. (a) Median grain size; (b) DRS hematite band position; (c) CIA; (d–f) K/Al vs. Ti/Al; (g–i) LREE/HREE; (j–l) Zr–Th–Sc.

The DRS band position (peaking coordinates) of hematite is affected by the substitution of isomorphous cations associated with the depositional environment; the higher the degrees of substitution, the lower the coordinate values [53]. Our results show that the band position of hematite is at approximately 580 nm for samples from Section 6, which indicates the presence of relatively stoichiometric hematite (Figure 7b). However, the upper samples have the hematite band position at around 550 nm, which strongly indicates that the hematite particles in the shallower depths are isomorphously substituted. The inconsistent features of the hematite band position for samples from the shallower depths between two soil profiles indicate that they could either be formed in different depositional environments and/or have distinct provenance origins.

The chemical index of alteration (CIA) can quantify the degree of chemical weathering (Figure 7c) [54]. The CIA values of the background soil profile rapidly increase at 0–90 cmbs and then stabilize, whereas those of the anomaly area slowly increase at 0–125 cmbs and start to stabilize at 125 cmbs. CIA values of sediments from Sections 2 and 4 are different in the anomaly area and background area, which indicates chemical weathering differences.

Geochemical methods can effectively reveal provenance changes via the migration of active elements and enrichment of stable elements [20,55]. Among the major elements, Ti has very low solubility and strong weathering resistance, basically does not migrate during sediment transport and accumulation, and retains the characteristics of the original rock. Similarly, Al solubility is also low and generally does not migrate. The Ti/Al ratio can thus eliminate the interference of particle size sorting and reflect source rock information [56]. The K/Al ratio also shows significant differences for different minerals and can indicate the intensity of chemical action and, therefore, the provenance. Rare earth elements (REE) are ubiquitous in various rocks and reflect different sources and formation mechanisms. REE are generally stable and tend to change very little during weathering, transport, and deposition. REE can be divided into light rare earth elements (LREE) (La, Ce, Pr, Nd, Pm, Sm, and Eu) and heavy rare earth elements (HREE) (Gd, Tb, Dy, Ho, Er, Tm, Yb, Lu, and Y). The LREE/HREE ratio can reflect the degree of REE differentiation, which is an indicator of provenance. Among the trace elements, Zr is mainly enriched in zircon with a strong resistance to weathering and remains basically unaffected by weathering during transport and deposition. Th and Sc are also stable elements with low mobility and generally do not leach under extremely strong weathering conditions. Zr, Th, and Sc are also relatively insoluble during weathering, erosion, transfer, and deposition, and do not significantly fractionate; thus, their combination is suitable for indicating provenance. K/Al versus Ti/Al (Figure 7d–f), LREE/HREE (Figure 7g–i), and Zr–Th–Sc (Figure 7j–l) for samples in Sections 2 and 4 from the background and anomaly areas belong to different scopes with no intersection, which reflects different provenances, while that in Section 6 from both areas are very similar and overlap, which indicates consistent provenance.

5. Discussion

Integrated methods and interdisciplinary research have achieved optimistic results in some large-scale prospecting projects (e.g., geological structures and commercial mineral development) [57–62]. However, the application of an integrated concept still needs further development and innovation in archaeological exploration [2,10,63], mainly owing to the scale and attributes of the detected targets. Compared with mineral deposits, magnetic anomalies caused by archaeological sites generally have smaller scales and lower intensities. In addition, archaeological sites often show regular shapes and distributions [9,15,21]. These features not only impose higher accuracy requirements for the detection equipment, but also require more diverse experimental methods to provide constraints on the target analysis. With the advancement of detection equipment, as well as the development of scientific and technological archaeological concepts, the effectiveness and efficiency of instruments have continuously improved and the analysis methods and indicators have been constantly enriched [4,24,64–66]. These improvements provide favorable conditions for the application of method integration in archaeological research.

This research is a new attempt at applying integrated methods and interdisciplinarity to the field of archaeology in cooperation with the archaeological team. We hope to establish comprehensive pre-archaeological exploration by integrating advanced magnetic surveys and various sample analyses. This integrated mode has the following advantages. (1) The UAV aeromagnetic system can overcome the complex landforms to carry out magnetic surveys in the study area. The survey results may be restricted by ambiguities in data interpretation, but they can provide positional guidance for further exploration and soil sampling. (2) The vertical sampling technology with small-caliber probes can quickly and flexibly obtain soil samples from different depths in potential target areas (identified based on magnetic survey results or archaeological sites). (3) Comprehensive analyses of soil samples can provide multiple constraints on UAV magnetic survey results. On the one hand, rock (mineral) magnetic results can further verify the magnetic difference between the aeromagnetic anomaly area and the background area and also provide constraints on the depth of difference. On the other hand, a sedimentary environment and the provenance information can provide constraints for the archaeological interpretation of aeromagnetic

anomalies. (4) The integrated mode has a progressive process; the use of different disciplines gives consistency to the archaeological study and validity to the magnetic alterations detected by the UAV.

The integrated pre-archaeological survey has been successfully applied to an archaeological area in Huizhou. The results provide multiple lines of evidence for identifying and evaluating potential archaeological targets. First, two repeated aeromagnetic surveys (along different directions) confirm the existence and consistency of the position of anomaly G. Second, rock magnetic analysis shows that the anomaly G and background areas have different magnetic mineral properties (e.g., concentration, grain size, and type) at the target depth horizon (0–150 cm), which is consistent with past archaeological cases [1–3,10,12–15,18,21]. Third, sedimentology and geochemical analyses show that the anomaly G and background areas may have experienced different sedimentary environments, and there are also differences in the provenance information.

Recent archaeological progress has verified the reliability of integrated pre-archaeological surveys (Figure 8) and the discovery of ancient city walls further confirms the archaeological value of anomaly G. The field survey found a section of an ancient city wall exposed on the northern edge of the square (Figure 8a), and its location and extension direction are consistent with the square edge (Figure 8b). The other edges of this square are also regular and covered with sparse vegetation (Figure 8d), which differs from the dense vegetation on both sides. This phenomenon might be due to the inhibitory effect of the city wall on plants and can be considered as “crop-marks”.

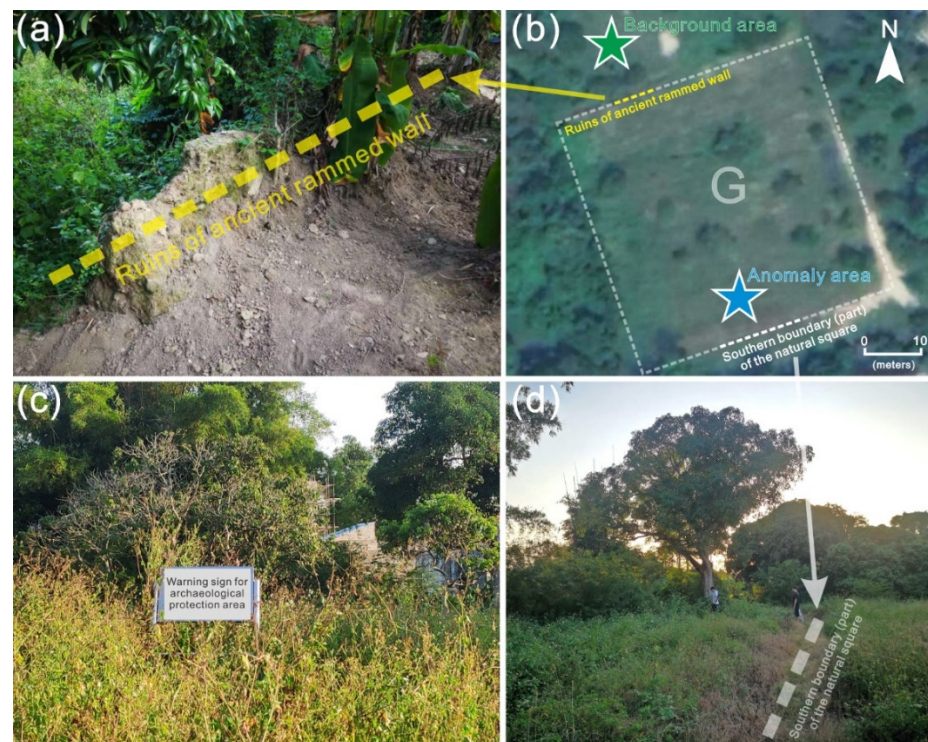


Figure 8. Archaeological progress and discoveries in G area. (a) The ruins of the ancient city wall are located on the northern edge of G area; (b) the special square landform of G area with sampling sites and locations of ruins; (c) an archaeological protection area has been established in this region; (d) difference in vegetation at the southern boundary of G area.

Previous studies showed that archaeological sites may produce either positive or negative anomalies [2,67,68]. In this study, integrated analysis of rock magnetism and geochemistry provide more constraints and evidence to discuss the possible causes of anomaly G. Geochemical proxies indicate that the provenance of soil in potential archaeological site (G) is different from that in the surrounding background region. This difference

can significantly result in distinct magnetic properties for soil samples from the archaeological site and further affect the induced and remanent magnetization [2]. Specifically, the induced magnetization is mainly affected by susceptibility. Most topsoil exhibits an enhancement of magnetic susceptibility in a natural environment; this phenomenon may be caused by climate (e.g., rainfall and wind) and sedimentary processes [69,70], especially the subtropical monsoon climate (warm and high precipitation) in our studied area. In contrast, the materials of an archaeological structure might come from other regions with low susceptibility and thus cause negative anomalies (induced magnetization). Moreover, a negative magnetic anomaly could also appear whenever there is an excavated pit that was immediately refilled by different materials [2,67], and this process often occurs in the construction of ancient city and archaeological structures. The original sedimentary formation may be randomized by the reburial process and, hence, diminish the remanent magnetization, and it would be more pronounced when filled by weak magnetism (e.g., ARM, SIRM) material similar to this study. In addition, there are also many kinds of remanence that can affect magnetic anomalies in archaeological sites [10,12,13,21]. However, more information on the buried structures is required to explore the exact connection between the anomaly and archaeological site [2]; further archaeological excavation would be helpful, but is not allowed at this stage.

This new integrated pre-archaeological survey provides an interdisciplinary concept for archaeology study, but we note that the exact application of methods should be adjusted according to the actual conditions of the survey areas. For example, when the survey area is difficult to access and, thus, ground survey work is not feasible, using UAV drone-mounted magnetometry for magnetic reconnaissance is achievable, and this method is more rapid and flexible than the traditional aeromagnetic survey. However, it is required to fly at a safe height to avoid hitting obstacles, which could limit its accuracy and make it difficult to map individual buried structures. When the survey area has suitable terrain (open, flat, and lacking vegetation), aeromagnetic surveys can be performed at different altitudes to obtain more detailed data. In terms of soil sample analysis, abundant drillings (soil samples) and pertinent excavations can provide more information and direct evidence for interpreting survey results, but sampling (excavating) work should be carried out with permission and in conjunction with archaeological exploration planning. In summary, the integrated method suggested in this study is flexible and has great application potential. In future, more advanced equipment and diversified analytical experiments can be further integrated for pre-archaeological surveys and provide more efficient and comprehensive support for tracking human civilization.

6. Conclusions

In this study, a comprehensive pre-archaeological exploration conducted by integrating advanced magnetic surveys and soil analyses has been performed on a potential archaeological site in Huizhou, China. Aeromagnetic analysis identified a negative magnetic anomaly in the studied area. Soil analyses verify that the negative magnetic anomaly area is magnetically and geochemically different from the surrounding areas, in particular at the shallower depth, which indicates that soil in the magnetic anomaly area is likely to have an exotic material source and, thus, be of archaeological value. The success of a UAV magnetic survey in identifying a potential archaeological site, together with its superior flexibility and efficiency, makes it worthy in archaeological investigations. In future, more advanced solutions and analytical methods will contribute to comprehensive pre-archaeological surveys and provide more support and information for archaeological investigation.

Author Contributions: Conceptualization, Q.L. and D.G.; methodology, H.Q., W.C. and X.X.; formal analysis, W.C., Z.J., Y.Z., J.L., Y.L. and X.J.; investigation, W.C., H.Q., C.L. and S.C.; writing—original draft preparation, W.C., Y.Z., J.L., Y.L. and X.J.; writing—review and editing, Q.L., Z.J., X.X., D.G., H.Q., C.L. and S.C.; supervision, Q.L., X.X. and D.G.; project administration, Q.L. and D.G. All authors have read and agreed to the published version of the manuscript.

Funding: This work was funded by the National Natural Science Foundation of China (41922026, 92158208, 41874078, 41704068, 42104068, and 41806063), the National Key Research and Development Program of China (2016YFA061903), the Shenzhen Science and Technology Program (KQTD20170810111725321, KCXFZ20211020174803005), and the opening foundation (SSKP202101) of the Shanghai She-shan National Geophysical Observatory (Shanghai, China), China Postdoctoral Science Foundation (2020M682770).

Institutional Review Board Statement: Not applicable.

Informed Consent Statement: Not applicable.

Data Availability Statement: The data presented in this study are contained within the article.

Acknowledgments: We are grateful to GTK (Shenzhen) Technology Co., Ltd., Guangdong Provincial Institute of Cultural Relics and Archaeology, for their help and cooperation. We thank Deting Yang and Wei Liu (CM2) for their assistance in field collection work, Yongxin Wang and Mengran Xin (SUSTech) for participating in experiments, and Congcong Gai, Haosen Wang, Weijie Zhang, Hai Li, and Huihui Yang (CM2) for helpful discussions.

Conflicts of Interest: The authors declare no conflict of interest.

References

1. Capozzoli, L.; De Martino, G.; Capozzoli, V.; Duploux, A.; Henning, A.; Rizzo, E. The pre-Roman hilltop settlement of Monte Torretta di Pietragalla: Preliminary results of the geophysical survey. *Archaeol. Prospect.* **2020**, *1*, 1–14. [[CrossRef](#)]
2. Fassbinder, J.W.E. Seeing beneath the farmland, steppe and desert soil: Magnetic prospecting and soil magnetism. *J. Archaeol. Sci.* **2015**, *56*, 85–95. [[CrossRef](#)]
3. Jordanova, N.; Jordanova, D.; Tcherkezova, E.; Popov, H.; Mokreva, A.; Georgiev, P.; Stoychev, R. Identification and Classification of Archeological Materials From Bronze Age Gold Mining Site Ada Tepe (Bulgaria) Using Rock Magnetism. *Geochem. Geophys. Geosyst.* **2020**, *21*, e2020GC009374. [[CrossRef](#)]
4. Bigman, D.P.; Day, D.J.; Balco, W.M. The roles of macro- and micro-scale geophysical investigations to guide and monitor excavations at a Middle Woodland site in northern Georgia, USA. *Archaeol. Prospect.* **2022**, *29*, 243–257. [[CrossRef](#)]
5. Derda, T.; Gwiazda, M.; Misiewicz, K.; Malkowski, W. Marea/Northern Hawwariya in northern Egypt: Integrated results of non-invasive and excavation works. *Archaeol. Prospect.* **2021**, *28*, 123–136. [[CrossRef](#)]
6. Pro, C.; Caldeira, B.; de Tena, M.T.; Charro, C.; Oliveira, R.J.; Borges, J.F.; Mayoral, V. Exploring the Consistency of Data Collected in Archaeological Geophysics: A Case Study from the Iron Age Hillfort of Villasviejas del Tamuja (Extremadura, Spain). *Remote Sens.* **2020**, *12*, 1989. [[CrossRef](#)]
7. Aveling, E. Archaeology-Magnetic trace of a giant henge. *Nature* **1997**, *390*, 232–233. [[CrossRef](#)]
8. Carrancho, A.; Villalain, J.J.; Vallverdu, J.; Carbonell, E. Is it possible to identify temporal differences among combustion features in Middle Palaeolithic palimpsests? The archaeomagnetic evidence: A case study from level O at the Abric Romani rock-shelter (Capellades, Spain). *Quat. Int.* **2016**, *417*, 39–50. [[CrossRef](#)]
9. Fassbinder, J. Magnetometry for archaeologists. *Archaeol. Prospect.* **2010**, *17*, 271–272. [[CrossRef](#)]
10. Maki, D. Lightning strikes and prehistoric ovens: Determining the source of magnetic anomalies using techniques of environmental magnetism. *Geoarchaeol.-Int. J.* **2005**, *20*, 449–459. [[CrossRef](#)]
11. Schmidt, V.; Becken, M.; Schmalzl, J. A UAV-borne magnetic survey for archaeological prospection of a Celtic burial site. *First Break* **2020**, *38*, 61–66. [[CrossRef](#)]
12. Birch, T.; Scholger, R.; Walach, G.; Stremke, F.; Cech, B. Finding the invisible smelt: Using experimental archaeology to critically evaluate fieldwork methods applied to bloomery iron production remains. *Archaeol. Anthropol. Sci.* **2015**, *7*, 73–87. [[CrossRef](#)]
13. Costanzo-Alvarez, V.; Suarez, N.; Aldana, M.; Hernandez, M.C.; Campos, C. Preliminary dielectric and rock magnetic results for a set of prehistoric Amerindian pottery samples from different Venezuelan Islands. *Earth Planets Space* **2006**, *58*, 1423–1431. [[CrossRef](#)]
14. Rosendahl, D.; Lowe, K.M.; Wallis, L.A.; Ulm, S. Integrating geoaerology and magnetic susceptibility at three shell mounds: A pilot study from Mornington Island, Gulf of Carpentaria, Australia. *J. Archaeol. Sci.* **2014**, *49*, 21–32. [[CrossRef](#)]
15. Tite, M.s.; Mullins, C. Enhancement of the Magnetic Susceptibility of Soil on Archaeological Sites. *Archaeometry* **1971**, *13*, 209–219. [[CrossRef](#)]
16. Cheyney, S.; Fishwick, S.; Hill, I.A.; Linford, N.T. Successful adaptation of three-dimensional inversion methodologies for archaeological-scale, total-field magnetic data sets. *Geophys. J. Int.* **2015**, *202*, 1271–1288. [[CrossRef](#)]
17. Pickartz, N.; Rabbel, W.; Rassmann, K.; Hofmann, R.; Ohlrau, R.; Thorwart, M.; Wilken, D.; Wunderlich, T.; Videiko, M.; Mueller, J. Inverse Filtering of Magnetic Prospection Data-A Gateway to the Social Structure of Cucuteni-Tripolye Settlements? *Remote Sens.* **2022**, *14*, 484. [[CrossRef](#)]
18. Smekalova, T.; Bevan, B.; Kashuba, M.; Lisetskii, F.; Borisov, A.; Kashirskaya, N. Magnetic surveys locate Late Bronze Age corrals. *Archaeol. Prospect.* **2021**, *28*, 3–16. [[CrossRef](#)]

19. Karamitrou, A.; Bogiatzis, P.; Tsokas, G.N. Fusion of geophysical images in the study of archaeological sites. *Archaeol. Prospect.* **2020**, *27*, 119–133. [[CrossRef](#)]
20. Maher, B.A.; Mutch, T.J.; Cunningham, D. Magnetic and geochemical characteristics of Gobi Desert surface sediments: Implications for provenance of the Chinese Loess Plateau. *Geology* **2009**, *37*, 279–282. [[CrossRef](#)]
21. Kosterov, A.; Kovacheva, M.; Kostadinova-Avramova, M.; Minaev, P.; Salnaia, N.; Surovitskii, L.; Yanson, S.; Sergienko, E.; Kharitonskii, P. High-coercivity magnetic minerals in archaeological baked clay and bricks. *Geophys. J. Int.* **2021**, *224*, 1257–1272. [[CrossRef](#)]
22. Gavazzi, B.; Le Maire, P.; de Lepinay, J.M.; Calou, P.; Munschya, M. Fluxgate three-component magnetometers for cost-effective ground, UAV and airborne magnetic surveys for industrial and academic geoscience applications and comparison with current industrial standards through case studies. *Geomech. Energy Environ.* **2019**, *20*, 100117. [[CrossRef](#)]
23. He, X.; Yang, X.; Luo, Z.; Guan, T. Application of unmanned aerial vehicle (UAV) thermal infrared remote sensing to identify coal fires in the Huojitu coal mine in Shenmu city, China. *Sci. Rep.* **2020**, *10*, 13895. [[CrossRef](#)]
24. Kolster, M.E.; Døssing, A. Scalar magnetic difference inversion applied to UAV-based UXO detection. *Geophys. J. Int.* **2021**, *224*, 468–486. [[CrossRef](#)]
25. Li, Z.P.; Gao, S.; Wang, X.B. New method of aeromagnetic surveys with rotorcraft UAV in particular areas. *Chin. J. Geophys.-Chin. Ed.* **2018**, *61*, 3825–3834. [[CrossRef](#)]
26. Zheng, Y.X.; Li, S.Y.; Xing, K.; Zhang, X.J. Unmanned Aerial Vehicles for Magnetic Surveys: A Review on Platform Selection and Interference Suppression. *Drones* **2021**, *5*, 93. [[CrossRef](#)]
27. King, J.W.; Channell, J.E.T. Sedimentary magnetism, environmental magnetism, and magnetostratigraphy. *Rev. Geophys.* **1991**, *29*, 358–370. [[CrossRef](#)]
28. Oldfield, F. Environmental Magnetism—A Personal Perspective. *Quat. Sci. Rev.* **1991**, *10*, 73–85. [[CrossRef](#)]
29. Vandenberghe, J.; Sun, Y.; Wang, X.; Abels, H.A.; Liu, X. Grain-size characterization of reworked fine-grained aeolian deposits. *Earth-Sci. Rev.* **2018**, *177*, 43–52. [[CrossRef](#)]
30. Ye, D. The geographical environment for developing foreign-oriented economy in huizhou municipality. *Trop. Geogr.* **1990**, *10*, 69–77.
31. Kuang, J.; Qi, S.; Wang, S.; Xiao, Z.; Zhang, M.; Zhao, X.; Gan, H. Granite Intrusion in Huizhou, Guangdong Province and Its Geothermal Implications. *Earth Sci.* **2020**, *45*, 1466–1480. [[CrossRef](#)]
32. Zhang, M.; Kuang, J.; Xiao, Z.C.; Wang, S.; Qi, S.H.; Chen, X.X. Geological Evolution since the Yanshanian in Huizhou, Guangdong Province: New Implications for the Tectonics of South China. *Earth Sci.* **2021**, *46*, 242–258. [[CrossRef](#)]
33. Zhang, Y. The Archaeological Discovery and its Value in Huizhou's Neolithic Age and the Spring and Autumn Warring Period. *J. Huizhou Univ.* **2018**, *38*, 41–46.
34. Zheng, H.; Zheng, C. The Boundary State Built by Luo Yue during the Shang and Zhou Dynasties-Luo Yue Cultural Research Series (twenty). *J. Guangxi Inst. Soc.* **2020**, *31*, 93–96.
35. Cheng, L. The Bronze Civilization in Lingnan-Hengling Mountain Cemetery Reveals the Secret of the Ancient Fulou Country. *Pop. Archaeol.* **2016**, *1*, 79–83.
36. Alken, P.; Thébaud, E.; Beggan, C.D.; Amit, H.; Aubert, J.; Baerenzung, J.; Bondar, T.N.; Brown, W.J.; Califf, S.; Chambodut, A.; et al. International Geomagnetic Reference Field: The thirteenth generation. *Earth Planets Space* **2021**, *73*, 49. [[CrossRef](#)]
37. Chen, H.Y.; Wang, R.; Miao, M.; Liu, X.C.; Ma, Y.H.; Hattori, K.; Han, P. A Statistical Study of the Correlation between Geomagnetic Storms and $M \geq 7.0$ Global Earthquakes during 1957–2020. *Entropy* **2020**, *22*, 1270. [[CrossRef](#)]
38. Stewart, I.C.F. A simple approximation for low-latitude magnetic reduction-to-the-pole. *J. Appl. Geophys.* **2019**, *166*, 57–67. [[CrossRef](#)]
39. Jiabo, L. PyIRM. Available online: <https://github.com/botaoxiongyong/pyIRM> (accessed on 16 July 2022).
40. Harrison, R.J.; Feinberg, J.M. FORCinel: An improved algorithm for calculating first-order reversal curve distributions using locally weighted regression smoothing. *Geochem. Geophys. Geosyst.* **2008**, *9*, Q05016. [[CrossRef](#)]
41. Torrent, J.; Barron, V. The visible diffuse reflectance spectrum in relation to the color and crystal properties of hematite. *Clays Clay Miner.* **2003**, *51*, 309–317. [[CrossRef](#)]
42. Lu, H.Y.; Xia, X.C.; Liu, J.Q.; Qin, X.G.; Wang, F.B.; Yidilisi, A.; Zhou, L.P.; Mu, G.J.; Jiao, Y.X.; Li, J.Z. A preliminary study of chronology for a newly-discovered ancient city and five archaeological sites in Lop Nor, China. *Chin. Sci. Bull.* **2010**, *55*, 63–71. [[CrossRef](#)]
43. Wu, T.H.; Xu, B.; Wang, X.R. How ancient Chinese constellations are applied in the city planning? An example on the planning principles employed in Xianyang, the capital city of Qin Dynasty. *Sci. Bull.* **2016**, *61*, 1634–1636. [[CrossRef](#)]
44. Oldfield, F.; Hunt, A.; Jones, M.D.H.; Chester, R.; Dearing, J.A.; Olsson, L.; Prospero, J.M. Magnetic Differentiation of Atmospheric Dusts. *Nature* **1985**, *317*, 516–518. [[CrossRef](#)]
45. Maher, B.A. Magnetic Properties of Some Synthetic Submicron Magnetites. *Geophys. J. Int.* **2007**, *94*, 83–96. [[CrossRef](#)]
46. King, J.; Banerjee, S.K.; Marvin, J.; Ozdemir, O. A comparison of different magnetic methods for determining the relative grain size of magnetite in natural materials: Some results from lake sediments. *Earth Planet. Sci. Lett.* **1982**, *59*, 404–419. [[CrossRef](#)]
47. Liu, Q.S.; Roberts, A.P.; Larrasoana, J.C.; Banerjee, S.K.; Guyodo, Y.; Tauxe, L.; Oldfield, F. Environmental magnetism: Principles and applications. *Rev. Geophys.* **2012**, *50*. [[CrossRef](#)]

48. Hrouda, F. A Technique for the Measurement of Thermal-Changes of Magnetic-Susceptibility of Weakly Magnetic Rocks by the Cs-2 Apparatus and Kly-2 Kappabridge. *Geophys. J. Int.* **1994**, *118*, 604–612. [[CrossRef](#)]
49. Heslop, D.; Dekkers, M.J.; Kruiver, P.P.; van Oorschot, I.H.M. Analysis of isothermal remanent magnetization acquisition curves using the expectation-maximization algorithm. *Geophys. J. Int.* **2002**, *148*, 58–64. [[CrossRef](#)]
50. Dunlop, D.J. Theory and application of the Day plot (M_{rs}/M_s versus H_{cr}/H_c) 1. Theoretical curves and tests using titanomagnetite data. *J. Geophys. Res.-Solid Earth* **2002**, *107*, 2056. [[CrossRef](#)]
51. Roberts, A.P.; Cui, Y.L.; Verosub, K.L. Wasp-waisted hysteresis loops: Mineral magnetic characteristics and discrimination of components in mixed magnetic systems. *J. Geophys. Res.-Solid Earth* **1995**, *100*, 17909–17924. [[CrossRef](#)]
52. Roberts, A.P.; Pike, C.R.; Verosub, K.L. First-order reversal curve diagrams: A new tool for characterizing the magnetic properties of natural samples. *J. Geophys. Res.-Solid Earth* **2000**, *105*, 28461–28475. [[CrossRef](#)]
53. Liu, Q.S.; Torrent, J.; Barron, V.; Duan, Z.Q.; Bloemendal, J. Quantification of hematite from the visible diffuse reflectance spectrum: Effects of aluminium substitution and grain morphology. *Clay Miner.* **2011**, *46*, 137–147. [[CrossRef](#)]
54. Nesbitt, H.W.; Young, G.M. Early Proterozoic Climates and Plate Motions Inferred from Major Element Chemistry of Lutites. *Nature* **1982**, *299*, 715–717. [[CrossRef](#)]
55. Wedepohl, K.H. The composition of the continental crust. *Geochim. Cosmochim. Acta* **1995**, *59*, 1217–1232. [[CrossRef](#)]
56. Sheldon, N.D.; Tabor, N.J. Quantitative paleoenvironmental and paleoclimatic reconstruction using paleosols. *Earth-Sci. Rev.* **2009**, *95*, 1–52. [[CrossRef](#)]
57. Blanco-Montenegro, I.; Montesinos, F.G.; Arnosó, J. Aeromagnetic anomalies reveal the link between magmatism and tectonics during the early formation of the Canary Islands. *Sci. Rep.* **2018**, *8*, 42. [[CrossRef](#)]
58. Khesin, B.; Feinstein, S.; Vapnik, Y.; Itkis, S.; Leonhardt, R. Magnetic study of metamorphosed sedimentary rocks of the Hatrumim formation, Israel. *Geophys. J. Int.* **2005**, *162*, 49–63. [[CrossRef](#)]
59. Leseane, K.; Betts, P.; Armit, R.; Ailleres, L. Structural overprinting criteria determined from regional aeromagnetic data: An example from the Hill End Trough, East Gondwana. *Tectonophysics* **2020**, *797*, 228660. [[CrossRef](#)]
60. Paoletti, V.; Gruber, S.; Varley, N.; D’Antonio, M.; Supper, R.; Motschka, K. Insights into the Structure and Surface Geology of Isla Socorro, Mexico, from Airborne Magnetic and Gamma-Ray Surveys. *Surv. Geophys.* **2016**, *37*, 601–623. [[CrossRef](#)]
61. Salapare, R.C.; Dimalanta, C.B.; Ramos, N.T.; Manalo, P.C.; Faustino-Eslava, D.V.; Queano, K.L.; Yumul, G.P. Upper crustal structure beneath the Zambales Ophiolite Complex, Luzon, Philippines inferred from integrated gravity, magnetic and geological data. *Geophys. J. Int.* **2015**, *201*, 1522–1533. [[CrossRef](#)]
62. Uwiduhaye, J.D.; Ngaruye, J.C.; Saibi, H. Defining potential mineral exploration targets from the interpretation of aeromagnetic data in western Rwanda. *Ore Geol. Rev.* **2021**, *128*, 103927. [[CrossRef](#)]
63. Diarte-Blasco, P.; Casas, A.M.; Pocovi, A.; Villalain, J.J.; Munoz, A.; Beolchini, V.; Pueyo-Anchuela, O.; Pena-Chocarro, L. Interpretation of magnetic anomalies of geological and archaeological origins in a volcanic area (Tusculum site, Lazio, Italy): Methodological proposals. *J. Appl. Geophys.* **2020**, *173*, 103942. [[CrossRef](#)]
64. Kaub, L.; Keller, G.; Bouligand, C.; Glen, J.M.G. Magnetic Surveys with Unmanned Aerial Systems: Software for Assessing and Comparing the Accuracy of Different Sensor Systems, Suspension Designs and Compensation Methods. *Geochem. Geophys. Geosyst.* **2021**, *22*, e2021GC009745. [[CrossRef](#)]
65. Taylor, J.M.; Cappellaro, P.; Childress, L.; Jiang, L.; Budker, D.; Hemmer, P.R.; Yacoby, A.; Walsworth, R.; Lukin, M.D. High-sensitivity diamond magnetometer with nanoscale resolution. *Nat. Phys.* **2008**, *4*, 810–816. [[CrossRef](#)]
66. Orengo, H.A.; Garcia-Molsosa, A.; Berganzo-Besga, I.; Landauer, J.; Aliende, P.; Tres-Martinez, S. New developments in drone-based automated surface survey: Towards a functional and effective survey system. *Archaeol. Prospect.* **2021**, *28*, 519–526. [[CrossRef](#)]
67. Fassbinder, J.; Irlinger, W. Magnetometerprospektion eines endneolithischen Grabenwerkes bei Riekofen. *Beiträge Archäol. Oberpfalz* **1998**, *2*, 47–54.
68. Quesnel, Y.; Jrad, A.; Mocci, F.; Gattacceca, J.; Mathe, P.E.; Parisot, J.C.; Hermitte, D.; Dumas, V.; Dussouillez, P.; Walsh, K.; et al. Geophysical Signatures of a Roman and Early Medieval Necropolis. *Archaeol. Prospect.* **2011**, *18*, 105–115. [[CrossRef](#)]
69. Dalan, R.A. A review of the role of magnetic susceptibility in archaeogeophysical studies in the USA: Recent developments and prospects. *Archaeol. Prospect.* **2008**, *15*, 1–31. [[CrossRef](#)]
70. Liu, Q.; Zhang, C.; Torrent, J.; Barrón, V.; Hu, P.; Jiang, Z.; Duan, Z. Factors Controlling Magnetism of Reddish Brown Soil Profiles from Calcarenites in Southern Spain: Dust Input or In-situ Pedogenesis? *Front. Earth Sci.* **2016**, *4*, 1–12. [[CrossRef](#)]